PIER C

(Received 20 March 2026, Accepted 24 April 2026, Scheduled 7 May 2026)

Study on Frequency Splitting and Segmented Tracking for High-Performance WPT under Horizontal Offset

Junjun Li[1], Jialin Zou[1], Yao Zou[1], and Zhongqi Li[1,2,*]

[1] *College of Transportation and Electrical Engineering, Hunan University of Technology, Zhuzhou 412000, China*
[2] *College of Electrical and Information Engineering, Hunan University, Changsha 410082, China*

ABSTRACT: Wireless power transfer systems suffer from frequency splitting and drift due to horizontal coil offset, which degrade both efficiency and output power. This paper derives a sixth-order equation to calculate resonant frequencies at the maximum efficiency point (Freq-MEP). The frequencies at the maximum power point (Freq-MPP) are determined by differentiating the output power with respect to the operating frequency. Both Freq-MEP and Freq-MPP are shown to vary with horizontal offset. Based on this analysis, a segmented frequency-tracking method is proposed to achieve simultaneous high efficiency and high output power under varying offset conditions. The effectiveness of the developed magnetic resonant WPT system is validated through numerical simulations and experiments.

1. INTRODUCTION

Magnetically coupled resonance wireless power transfer (WPT) systems are known for high efficiency and power output [1–3]. Hence, the WPT system is extensively utilised in numerous applications, including consumer electronics, medical devices, automated guided vehicles, and electric vehicle battery charging [3, 4]. However, variations in horizontal offset can cause frequency detuning and splitting, which significantly reduce both transmission efficiency and output power [5, 6]. Therefore, it is of great significance to study the frequency-splitting mechanism and the automatic frequency-tracking theory of wireless power transfer systems, thereby improving the efficiency and output power of WPT systems [7, 8].

To address the above problems, a power regulation method that controls the primary wireless power supply's frequency was proposed [9]. Experimental results demonstrated that this method effectively regulates the power delivered to the load across a wide range of load conditions. A combined frequency-tracking and impedance-matching system was proposed to mitigate the adverse effects of parameter variations on transmission efficiency [10]. When the load impedance was changed, the transmission efficiency increased, thereby optimising the source operating frequency. To improve transmission efficiency in the strong-coupling region, an automated frequency-tracking system was deployed in the WPT system. The proposed tracking system was designed to maintain transmission efficiency above 70% across all transfer distances by directly monitoring efficiency through out-of-band communication [11]. However, the above methods can only improve the system efficiency, but do not simultaneously optimize the output power under the condition of coil horizontal offset.

To further improve output power, an accurate frequency-tracking method based on direct phase control was proposed. The maximum transmission power can be obtained with the proposed frequency-tracking method [12]. To enhance output power in the strong-coupling region, an adaptive frequency-tracking control (AFTC) method, utilising a closed-loop control scheme, was implemented [13, 14]. Furthermore, an enhanced particle swarm optimisation algorithm was introduced alongside the AFTC to enable real-time tracking of the maximum power point [14]. In summary, there is no method to simultaneously increase system efficiency and output power when a horizontal offset between coils occurs.

This paper establishes the functional relationship between output power and frequency, as well as the expression linking horizontal offsets to the resonant frequency. The resonant frequencies at the maximum efficiency point (Freq-MEP) and at the maximum power point (Freq-MPP) can be determined. Additionally, a segmented frequency tracking method is proposed to achieve both high efficiency and high output power across various horizontal offsets.

The remainder of the paper is outlined as follows. Section 2 gives a mathematical model. Section 3 presents frequency calculation and simulation verification. Section 4 introduces the automatic frequency tracking method. Section 5 describes the experimental setup and presents the experimental values for different horizontal offsets. Section 6 concludes the study.

2. MATHEMATIC MODEL

Figure 1 illustrates the fundamental configuration of the wireless power transfer architecture, constructed using paired magnetically coupled resonant elements (transmitter Tx and receiver Rx coils) separated by air gap distance D, while C_{Tx} and C_{Rx} represent the external compensating capacitances for coils, respectively. Δ denotes the horizontal offset between the Tx and Rx coils. The WPT system can be modelled using lumped circuit elements (L, C, and R) [15, 16], as depicted in Figure 2.

* Corresponding author: Zhongqi Li (lizhongqi@hnu.edu.cn).

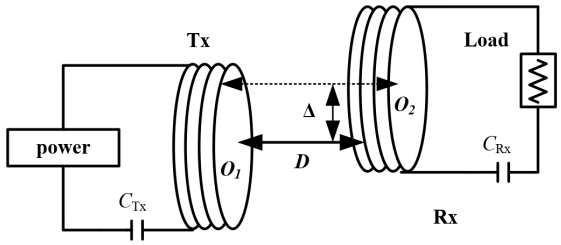

FIGURE 1. Simplified diagram of the wireless power transfer system utilizing magnetically coupled resonators.

In this model, V_s denotes the source power. The equivalent circuit model incorporates three distinct resistive components. R_1 is the transmitter winding loss; R_2 is the receiver winding loss; and R_S is the source impedance. System parameters include L_1 and L_2, which are the inductances of coils, and the mutual coupling coefficient M determines energy transfer efficiency. The input impedance characteristics are defined by Z_{in}, while frequency domains comprise ω_1 (transmitter resonance), ω_2 (receiver resonance), ω_0 (natural resonance), and ω (operational frequency).

The physical parameters of the WPT system are governed by Kirchhoff's circuit laws [17, 18]:

$$\begin{cases} Z_1 I_1 + j\omega M I_2 = V_s \\ j\omega M I_1 + Z_2 I_2 = 0 \end{cases} \tag{1}$$

$$\begin{cases} Z_1 = R_S + R_1 + j\omega L_1 + 1/(j\omega C_{Tx}) \\ Z_2 = R_L + R_2 + j\omega L_2 + 1/(j\omega C_{Rx}) \end{cases} \tag{2}$$

where I_1 and I_2 respectively denote the instantaneous currents flowing through Tx and Rx. The coil currents I_1 and I_2 are analytically resolved through the governing Equations (1)–(2).

$$\begin{cases} I_1 = \frac{V_s Z_2}{Z_1 Z_2 + (\omega M)^2} \\ I_2 = -\frac{j\omega M V_s}{Z_1 Z_2 + (\omega M)^2} \end{cases} \tag{3}$$

The power transfer efficiency of systems can be formulated as:

$$\eta = \left| \frac{I_2^2 R_L}{V_s I_1} \right| = \left| \frac{(\omega M)^2 R_L}{Z_1 {Z_2}^2 + (\omega M)^2 Z_2} \right| \tag{4}$$

Equation (2) is substituted into (4), resulting in the expression for efficiency given in (5).

$$\eta = \left| \frac{I_2^2 R_L}{V_s I_1} \right| = \left| \frac{U^2 U_L}{\left\{ (1 + U_s + j\varepsilon_1 Q_1)(1 + U_L + j\varepsilon_2 Q_2)^2 + (1 + U_L + j\varepsilon_2 Q_2) U^2 \right\}} \right| \tag{5}$$

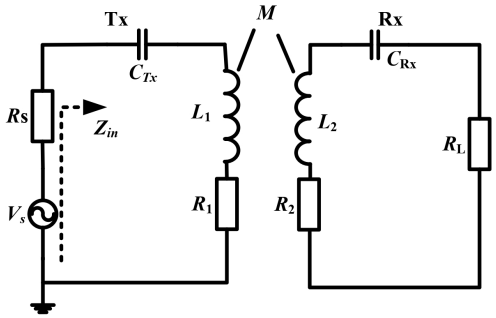

FIGURE 2. The equivalent circuit of the WPT system, where the coils are series resonators.

where the source matching factor is given by $U_s = R_s/R_1$; the load matching factor is expressed as $U_L = R_L/R_2$; the strong-coupling parameter is defined as $U = \omega M (R_1 R_2)^{1/2}$; the unloaded quality factor of the Tx coil is $Q_1 = \omega L_1/R_1$, and it is $Q_2 = \omega L_2/R_2$ for the Rx coil. The angular frequency deviation factor for the Tx coil is $\varepsilon_1 = 1 - \omega_1^2/\omega^2$, and it is $\varepsilon_2 = 1 - \omega_2^2/\omega^2$ for the Rx coil.

The expression of output power (6) is as follows:

$$P_{out} = |I_2^2 R_L| = \left| \frac{V_s U^2 U_L}{[(1+U_S+j\varepsilon_1 Q_1)\times(1+U_L+j\varepsilon_2 Q_2)+U^2]^2} \right| \tag{6}$$

By taking the derivative of P_{out} with respect to ω and setting the resulting function equal to zero

$$\frac{\partial P_{out}}{\partial \omega} = 0 \tag{7}$$

The angular Freq-MPP can be conveniently calculated using MATLAB, as shown in (7).

The input impedance is defined by (8).

$$Z_{in} = V_s/I_1 - R_s \tag{8}$$

By simultaneously solving Equations (2) and (8), the expression for the input impedance is derived as follows:

$$Z_{in} = R_1 \frac{\left\{ \left[(U^2 + (1+U_s)(1+U_L) - Q_1 Q_2 \varepsilon_1 \varepsilon_2) + j(Q_1 \varepsilon_1 (1+U_L) + Q_2 \varepsilon_2 (1+U_s)) \right] ((1+U_L) - jQ_2\varepsilon_2) \right\}}{(1+U_L)^2 + Q_2^2 \varepsilon_2^2} - R_s \tag{9}$$

Equation (9) can be simplified into (10).

$$Z_{in} = R_1 \frac{\left\{ \left[(1+U_L)^2 + U^2(1+U_L) + Q_2^2\varepsilon_2^2 \right] + j\left[(1+U_L)^2 Q_1 \varepsilon_1 + Q_1 \varepsilon_1 Q_2^2 \varepsilon_2^2 - U^2 Q_2^2 \varepsilon_2^2 \right] \right\}}{(1+U_L)^2 + Q_2^2 \varepsilon_2^2} \tag{10}$$

TABLE 1. Calculated Freq-MPP versus misalignments.

Misalignments/cm	Frequencies/kHz
0	77.165, 97.099
5	77.430, 96.572
10	78.331, 94.896
15	79.576, 92.798
20	80.945, 90.656
25	82.745, 88.309

Based on (10), the angle θ between the source voltage V_s and the current I_1 can be determined by analysing the phase difference between these two quantities as follows:

$$\theta = \arctan\left[\mathrm{Im}(Z_{in})/\mathrm{Re}(Z_{in})\right] = \arctan\left[\frac{(1+U_L)^2 Q_1\varepsilon_1 + Q_1 Q_2^2\varepsilon_1\varepsilon_2^2 - U^2 Q_2\varepsilon_2}{(1+U_L)^2 + U^2(1+U_L) + Q_2^2\varepsilon_2^2}\right] \quad (11)$$

Here $\mathrm{Re}(Z_{in})$ represents the real part of Z_{in} and $\mathrm{Im}(Z_{in})$ the imaginary part. Equation (12) can be derived from (11) with $\theta = 0$.

$$\left(L_1L_2^2 - L_2M^2\right)\omega^6 + \Big[(R_2+R_L)^2L_1 - 2L_1L_2^2\omega_2^2 - L_1L_2^2\omega_1^2 + L_2M^2\omega_2^2\Big]\omega^4 + \Big[L_1L_2^2\omega_2^4 + 2L_1L_2^2\omega_1^2\omega_2^2 - (R_2+R_L)^2L_1\omega_1^2\Big]\omega^2 - L_1L_2^2\omega_1^2\omega_2^4 = 0 \quad (12)$$

The operational resonance frequency characteristics of the wireless power transfer system are governed by the sixth-order polynomial solution of Equation (12). Parametric sensitivity analysis reveals frequency dependence on electromagnetic coupling (M), transmitter/receiver L_c parameters (C_{Tx}, L_1, C_{Rx}, L_2), and load impedance (R_L). While coil geometries maintain stable electrical properties, frequency deviations predominantly originate from mutual inductance variations induced by lateral displacement between coupled coils. Consequently, the resonant frequencies change as the horizontal offset shifts. In essence, Equation (12) allows the calculation of resonant frequencies while accounting for variations in coil parameters.

3. COMPUTATIONAL FREQUENCY ANALYSIS AND NUMERICAL VALIDATION

In this section, the Freq-MEP and Freq-MPP are calculated using Equations (12) and (7), respectively. The accuracy of Equations (12) and (7) is validated through MATLAB simulations. The results indicate that the system can display multiple resonant frequencies, and the frequency at which Freq-MEP occurs is nearly the same as that at which MPP is achieved, even with changes in horizontal offset. The system can operate simultaneously at both the MEP and the high-power operating point by adjusting the operating frequency.

TABLE 2. Calculated Freq-MEP versus misalignments.

Misalignments/cm	Frequencies/kHz
0	77.642, 85.292, 96.576
5	78.028, 85.292, 95.846
10	79.042, 85.291, 94.055
15	80.498, 85.286, 91.760
20	82.402, 85.272, 89.169
25	85.362

TABLE 3. Parameters of coils.

Symbol	Value
L_1	353.68 µH
L_2	216.02 µH
C_1	9.86 nF
C_2	16.09 nF
R_1	0.438 Ω
R_2	0.281 Ω
f_0	85.0 kHz

3.1. Frequency Calculation

According to (7), the Freq-MPP is calculated using MATLAB. Table 1 presents the Freq-MPP for different horizontal offsets. Due to frequency splitting, the system may exhibit two maximum output power points, and the corresponding Freq-MPP varies with misalignments.

Similarly, the Freq-MEP is calculated using Equation (12) with MATLAB. Table 2 displays the Freq-MEP for various horizontal offsets. The system may exhibit multiple maximum efficiencies, and the corresponding Freq-MEP also varies with misalignments. The coil parameters used in the calculation are provided in Table 3.

3.2. Simulation Verification

Numerical validation of the theoretical models is implemented via electromagnetic field simulations in the MATLAB/Simulink environment. The multi-physics simulation results are illustrated in Figure 3, which reveals three fundamental operational characteristics. Figure 3(a) depicts the impedance phase-frequency response under lateral displacement, presenting multiple zero-phase crossings ($\theta = 0$) corresponding to different resonance modes, which verifies the frequency splitting characteristics predicted by the theoretical model. Figure 3(b) shows the energy conversion efficiency spectrum, where the peak efficiency values correspond to the identified resonance frequencies, confirming the theoretical correlation between optimal efficiency and electromagnetic coupling states. Figure 3(c) presents the power transmission characteristics with a dual-peak behavior, and the maximum power frequencies are consistent with the analytical predictions of the proposed model. As the horizontal offset increases, the mutual inductance between coils decreases, and the system transforms from a strongly coupled state to a weakly coupled

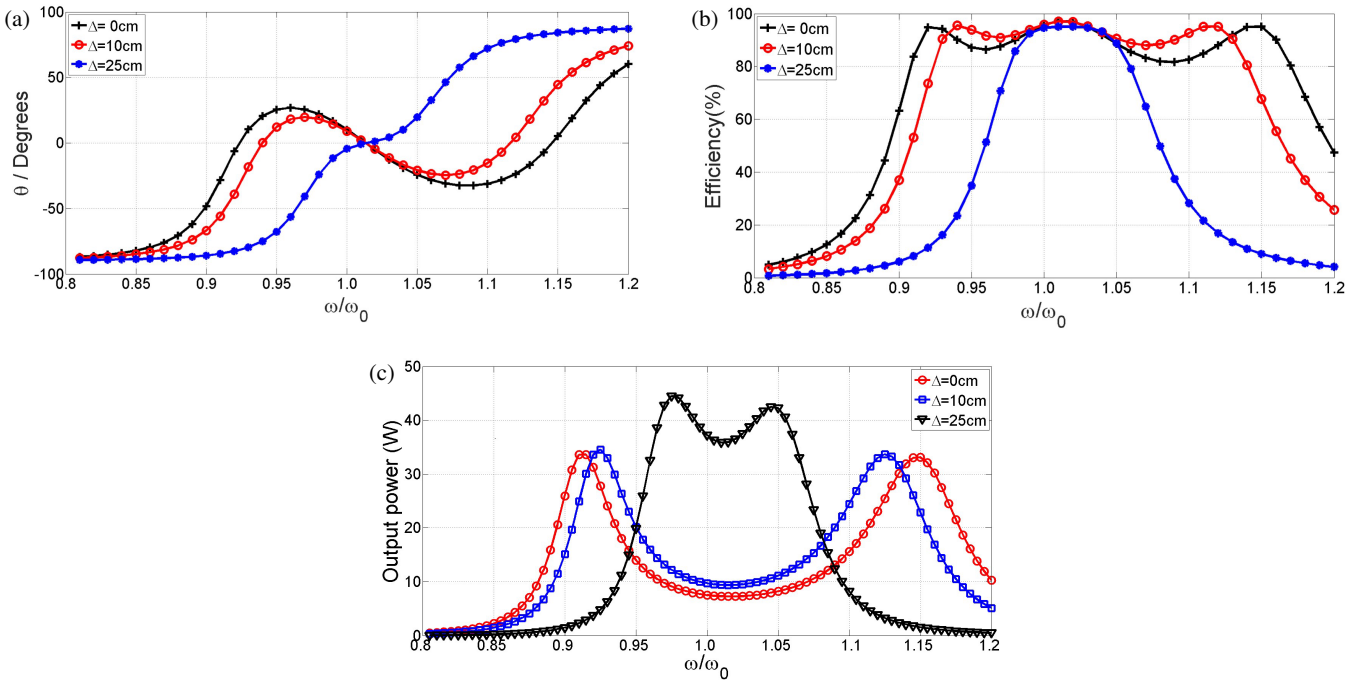

FIGURE 3. θ, efficiency, and output power as functions of ω/ω_0 for different horizontal offsets. (a) θ. (b) Efficiency. (c) Output power.

state, thus suppressing the frequency splitting of the WPT system. Multiple high-efficiency points in the system correspond to the resonant frequencies, while the output power presents a power-splitting feature with multiple high-power points near the resonant frequencies. The power at the initial resonant frequency is significantly lower than that at the adjacent resonant frequencies. Therefore, the resonant frequency must be adjusted to achieve the maximum efficiency and output power simultaneously.

4. METHOD OF AUTOMATIC FREQUENCY TRACKING

The preceding analysis establishes a parametric relationship between variations in horizontal offset and the frequency-splitting characteristics. Experimental results show that electromagnetic coupling disruptions caused by horizontal offset simultaneously affect both the optimal energy conversion frequencies and the maximum power transmission bands by dynamically modulating the excitation source frequency. The proposed architecture demonstrates dual-objective optimisation, enabling simultaneous peak efficiency and improved power delivery across various misalignment scenarios.

Figure 4 presents the schematic of the segmented frequency tracking method, primarily composed of a phase detector, the segmented frequency tracking algorithm, and a pulse frequency modulation (PFM) waveform generator. The methodology implements the workflow through the following operational sequence:

1) The input voltage V_s and current I_1 of Tx are measured by a voltage transformer and a current transformer, respectively.

2) The input voltage and current are converted into square wave signals.

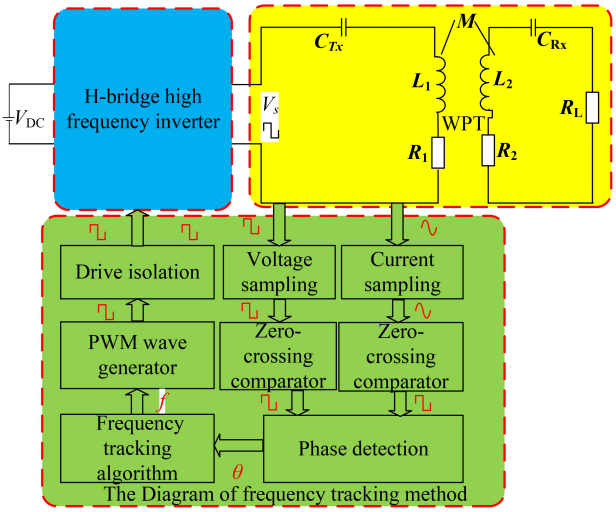

FIGURE 4. The illustration of the frequency tracking technique.

3) The phase detection principle involves calculating the value of θ by comparing the rising edges of the V_s signal and I_1 signal.

4) Adaptive frequency sweeping executes until impedance phase congruence is achieved, establishing optimal power transfer frequency.

5) The pulse width modulation (PWM) drive signal of the H-bridge can be obtained according to the resonant frequency and the PWM generator.

The flowchart of the segmented frequency tracking method is illustrated in Figure 5.

1) The frequency range is divided into two segments with 85 kHz as the boundary. The left segment covers 75 kHz–85 kHz (bandwidth of 10 kHz), and the right segment covers

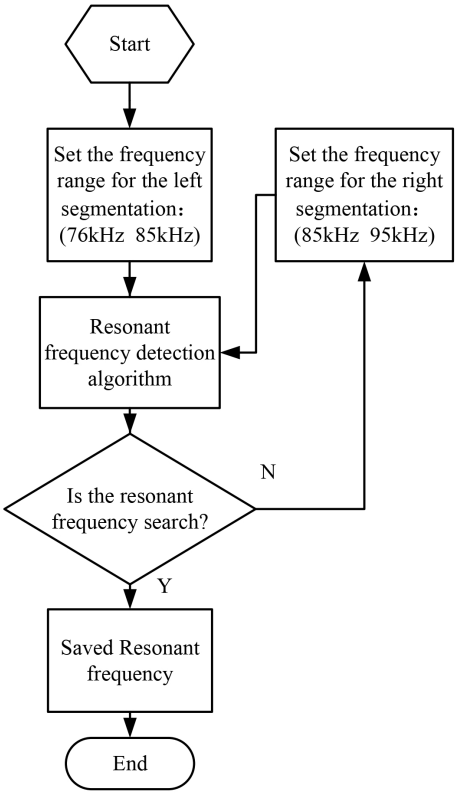

FIGURE 5. Algorithm flowchart.

85 kHz–98 kHz (bandwidth of 13 kHz). Since the left segment has a smaller range while maintaining comparable output power and efficiency, it is prioritized for faster and more accurate resonance tracking.

2) The search starts in the left segment (75 kHz–85 kHz). A $\pm 1^\circ$ phase difference tolerance is allowed due to phase detector error. Resonance is confirmed when $-1^\circ < \theta < 1^\circ$, and the system locks the frequency and exits. If no resonance is found, the algorithm proceeds to the right segment.

3) If resonance is not detected in the left segment, the search continues in the right segment (85 kHz–98 kHz). The frequency tracking algorithm is restarted, and the process terminates once the resonant point is identified and recorded.

Figure 6 illustrates the algorithm used to search for the resonant frequency.

Step 1. Initialisation: The starting frequency is set to 76 kHz when the left segmentation is used and to 95 kHz when the right segmentation is used.

Step 2. Setting the frequency range: The left segmentation frequency is varied from 76 kHz to 85 kHz. The optimal segmentation frequency within the frequency range is 85–95 kHz.

Step 3. Calculate the input impedance characteristic angle through phase detection.

Step 4. Frequency judgment: if $f \geq 85$ kHz, the left segmentation frequency of the algorithm is ended. If $f \leq 85$ kHz, the right segmentation frequency of the algorithm is reached.

Step 5. Input impedance characteristic angle judgment: If -1 degree $\leq \theta \leq 1$ degree, the resonant frequency is searched; else the frequency is automatically increased by 0.1 kHz, and the program returns to Step 3.

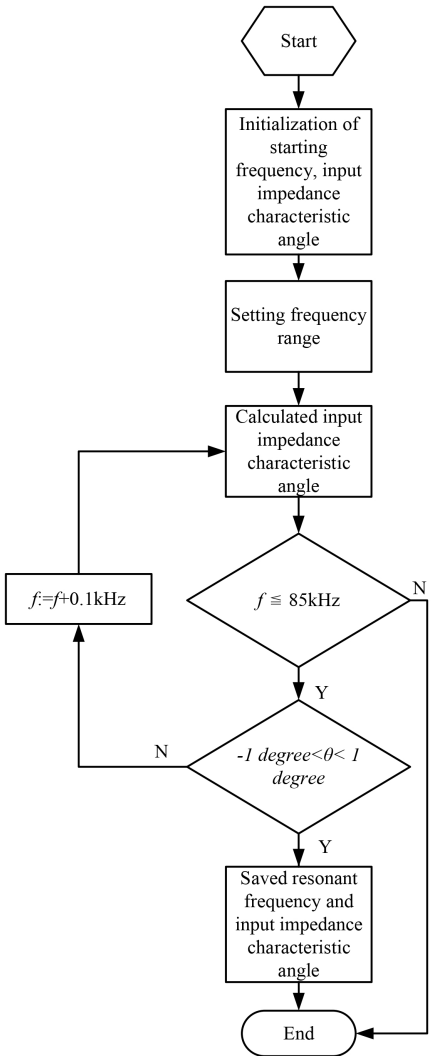

FIGURE 6. Flowchart of the algorithm of searching the resonant frequency.

5. RESULTS FROM EXPERIMENTS AND SIMULATIONS

A proof-of-concept prototype was implemented to verify the proposed methodology, with the system architecture illustrated in Figure 7. The proposed segmented frequency tracking algorithm is implemented on a TMS320F28335 digital signal processor (DSP), forming a closed-loop control with the PFM waveform generator, and full-bridge inverter, as shown in the control block diagram. The experimental configuration integrates five key subsystems: a DC power supply, a full-bridge switching converter, magnetically coupled resonant networks, an AC-DC converter module, and terminal-loading modules. A high-efficiency switching array consisting of four SiC MOSFETs operates in full-bridge mode within the transmitting unit to generate the AC excitation waveform. The transmission coil features an outer diameter of 60 cm, a pitch of 0 cm, and approximately 17 turns, while the receiving coil has an outer diameter of 55 cm, a pitch of 0 cm, and approximately 13 turns. All coils are fabricated using 300-strand AWG 38 Litz wire. The coil parameters are derived from [19–21] and measured

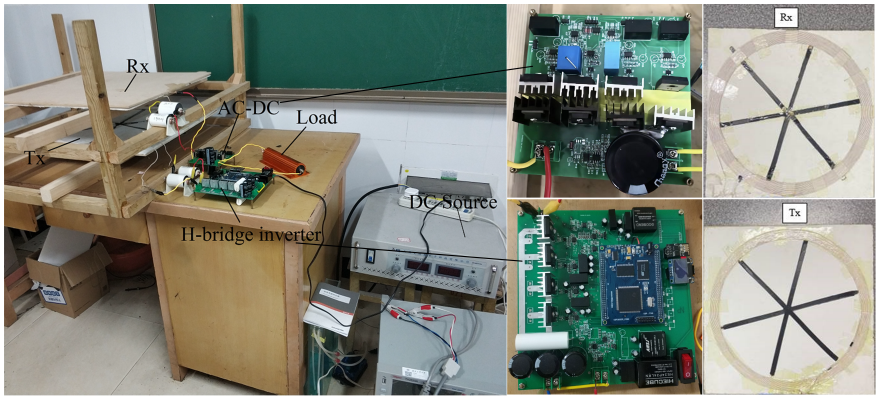

FIGURE 7. Experimental prototype setup.

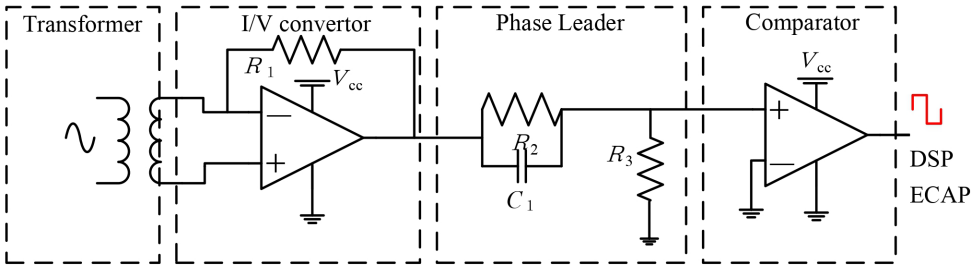

FIGURE 8. Phase detection subsystem.

using an impedance analyzer, following Equations (1) and (2). The experimental system operates at a baseline resonant frequency of 85.0 kHz with a 15 Ω load impedance and a 15 cm air gap. As listed in Table 3, the coupled inductor parameters enable ANSYS Maxwell-based electromagnetic modeling and practical verification of mutual inductance via impedance spectroscopy. The phase detection subsystem shown in Figure 8 employs analog-to-digital waveform conditioning and edge-detection logic, in which the phase angle is calculated by measuring the temporal offset between voltage and current signal transitions using the enhanced capture peripheral (ECAP). Figure 9 shows the variation of mutual inductance with lateral displacement, revealing a 55.3% reduction from 66.2 µH to 29.6 µH as the misalignment changes from coaxial to a 25 cm offset.

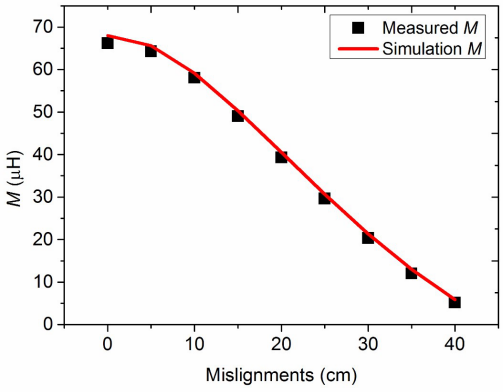

FIGURE 9. Measured and simulation M between Tx and Rx.

5.1. Frequency Testing

The resonant frequencies are determined by sweeping the impedance analyser across different horizontal offsets. The measured resonant frequencies are shown in Table 4. They agree with the calculated resonant frequencies.

TABLE 4. Calculated Freq-MPP versus misalignments.

Misalignments/cm	Frequencies/kHz
0	77.576, 85.194, 96.476
5	78.104, 85.305, 95.796
10	79.101, 85.314, 93.955
15	80.437, 85.317, 91.710
20	82.353, 85.214, 89.118
25	85.298

The switching frequency optimisation process involves sweeping the H-bridge PWM frequency while monitoring output characteristics. As tabulated in Table 5, experimentally determined peak efficiency frequencies show a strong correlation with theoretical resonance predictions.

5.2. Frequency Tracking Method Validation

The frequency tracking performance is validated under three representative lateral misalignment conditions ($\Delta = 0$ cm, 10 cm, and 25 cm). Using differential voltage probes and Hall-effect current sensors (100 mV/A conversion ratio), the primary-side voltage V_s and current I_s waveforms are cap-

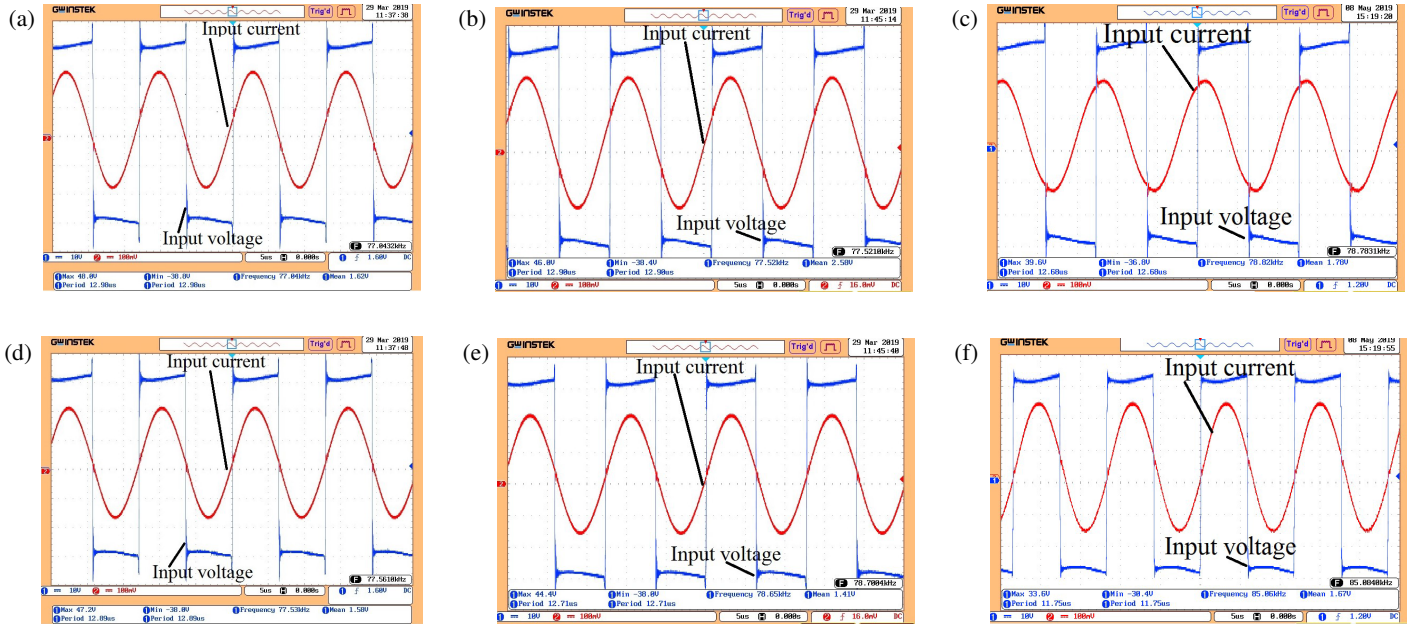

FIGURE 10. Primary-side voltage V_s and current I_s waveforms under different lateral misalignments. (a) $\Delta = 0$ cm without algorithm. (b) $\Delta = 10$ cm without algorithm. (c) $\Delta = 25$ cm without algorithm. (d) $\Delta = 0$ cm with algorithm. (e) $\Delta = 10$ cm with algorithm. (f) $\Delta = 25$ cm with algorithm.

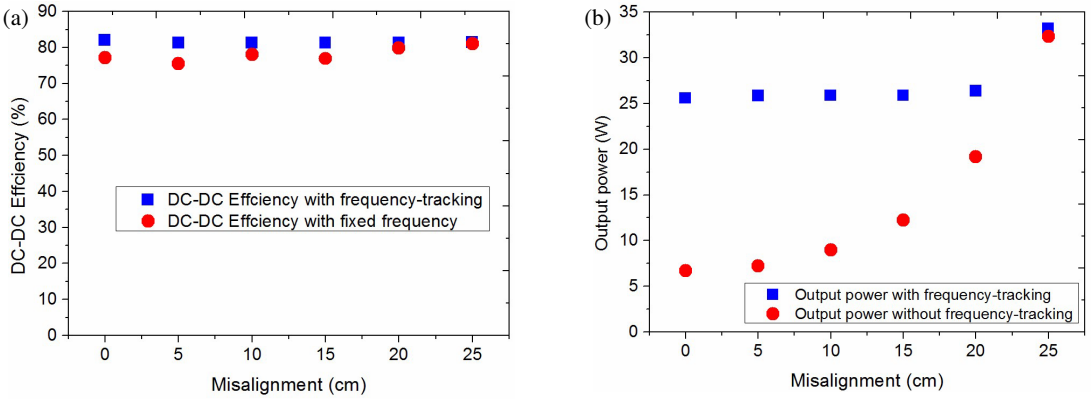

FIGURE 11. Measured efficiency and output power as a function of misalignment. (a) Efficiency. (b) Output power.

TABLE 5. Measured Freq-MPP versus misalignments.

Misalignments/cm	Frequencies/kHz
0	76.775, 96.897
5	76.931, 96.842
10	79.121, 95.196
15	79.887, 93.023
20	80.726, 90.126
25	81.941, 88.132

tured. Without the proposed algorithm, the system operates at a fixed frequency and exhibits significant phase shifts between voltage and current, indicating typical off-resonance behaviour, as shown in Figures 10(a)–(c). In contrast, the proposed frequency-adaptation algorithm dynamically adjusts the excitation frequency to achieve near-zero phase difference under each misalignment case: 77.56 kHz for $\Delta = 0$ cm, 78.70 kHz for $\Delta = 10$ cm, and 85.08 kHz for $\Delta = 25$ cm, as illustrated in Figures 10(d)–(f). These results confirm that the proposed method can effectively track the real-time resonant frequency and compensate for mutual inductance variations caused by variable lateral misalignment.

5.3. Output Power and Efficiency Test

Comparative experimental results validate the superior conversion efficiency and the power output of the proposed method when benchmarked against conventional fixed-frequency operation at 85 kHz. System performance is experimentally characterised across lateral displacement Δ ranging from 0 to 25 cm in 5 cm increments. As shown in Figure 11. In Figure 11(a), with adaptive frequency control, the system efficiency remains stable within 81.2% to 82.0%, significantly outperforming the

fixed-frequency mode (from 75.4% to 81.0%). At maximum displacement ($\Delta = 25$ cm), both methods exhibit comparable efficiency as the optimal frequency (85.298 kHz) approaches the baseline frequency. In Figure 11(b), measurements show that the proposed method improves output power under extreme misalignment by a factor of 3.8 compared to conventional fixed-frequency operation.

Under lateral displacement conditions (from 0 to 20 cm), the adaptive frequency strategy demonstrates stable power transfer characteristics with $< 2\%$ efficiency fluctuation (from 82.0% to 81.2%) and 76.7% power retention (from 33.2 W to 25.6 W). In contrast, fixed-frequency operation exhibits 79.8% power degradation (from 33.2 W to 6.7 W). The robustness of the proposed method against misalignment-induced coupling variations is verified under identical conditions.

6. CONCLUSION

This study presents a dual-frequency determination method for wireless power transfer systems, which can identify Freq-MEP and Freq-MPP simultaneously. The method is valid under arbitrary variations in transceiver coil parameters. Transverse displacement analysis shows that the system has multimodal characteristics; Freq-MEP and Freq-MPP are non-coincident and gradually approach the original resonance with increasing offset, demonstrating the system's adaptability to coupling degradation. The results support reasonable frequency selection for maximum efficiency or power. A segmented frequency tracking method is proposed to track the resonant frequency in real time under various horizontal offsets. The method achieves high efficiency and high output power simultaneously, offering a reliable solution for fast and efficient charging.

The current research focuses on fundamental tracking principles rather than convergence rate optimisation, owing to the fixed-step implementation. Future work will explore adaptive step-size control and improved generalization of the segmented frequency strategy to enhance response speed and applicability.

ACKNOWLEDGEMENT

This work was supported in part by the Natural Science Foundation of Hunan Province under Grants 2022JJ30226, National Key R&D Program Project (2022YFB3403200), Key Projects of Hunan Provincial Department of Education (23A0432), Excellent Youth Project of Scientific Research of Hunan Provincial Department of Education (22B0577), National Natural Science Foundation of China (NSFC) Youth Science Fund Project (62303178), and A Project Supported by Scientific Research Fund of Hunan Provincial Education Department (23C0182).

REFERENCES

[1] Sun, C., W. Yang, Y. He, C. Dong, X. Liang, Y. Wei, H. Chen, and N.-X. Sun, "Electrostatically tunable mutual inductance for frequency splitting elimination in wireless power transfer," *IEEE Transactions on Magnetics*, Vol. 58, No. 2, 1–6, 2022.

[2] Hua, Z., K. T. Chau, H. Pang, and T. Yang, "Dynamic wireless charging for electric vehicles with autonomous frequency control," *IEEE Transactions on Magnetics*, Vol. 59, No. 11, 1–5, 2023.

[3] Esse, A., K. Abdullah, M. H. Habaebi, and H. A. M. Ramli, "Dynamic power splitting simultaneous wireless information and power transfer split receiver for wireless sensor networks," *IEEE Access*, Vol. 9, 129 407–129 416, 2021.

[4] Song, M. S., H. Y. Lee, and G. S. Park, "Effect of coil shape on the critical load resistance of frequency splitting phenomenon in magnetic resonance wireless power transfer," *IEEE Transactions on Magnetics*, Vol. 60, No. 12, 1–4, 2024.

[5] Zhang, B., Y. Hu, W. Hu, and W. Han, "Power boosting of strongly coupled wireless power transfer systems by aligning 1st/3rd harmonic frequencies with splitting frequencies," *IEEE Transactions on Power Electronics*, Vol. 40, No. 7, 8917–8922, 2025.

[6] Narayanamoorthi, R., A. V. Juliet, and B. Chokkalingam, "Frequency splitting-based wireless power transfer and simultaneous propulsion generation to multiple micro-robots," *IEEE Sensors Journal*, Vol. 18, No. 13, 5566–5575, 2018.

[7] Ojukwu, H., B.-C. Seet, and S. U. Rehman, "Metasurface-aided wireless power transfer and energy harvesting for future wireless networks," *IEEE Access*, Vol. 10, 52 431–52 450, 2022.

[8] Liu, X., X. Yuan, C. Xia, and X. Wu, "Analysis and utilization of the frequency splitting phenomenon in wireless power transfer systems," *IEEE Transactions on Power Electronics*, Vol. 36, No. 4, 3840–3851, 2021.

[9] Si, P., A. P. Hu, S. Malpas, and D. Budgett, "A frequency control method for regulating wireless power to implantable devices," *IEEE Transactions on Biomedical Circuits and Systems*, Vol. 2, No. 1, 22–29, 2008.

[10] Luo, Y., Y. Yang, S. Chen, and X. Wen, "A frequency-tracking and impedance-matching combined system for robust wireless power transfer," *International Journal of Antennas and Propagation*, Vol. 2017, No. 1, 5719835, 2017.

[11] Kim, N. Y., K. Y. Kim, Y.-H. Ryu, J. Choi, D.-Z. Kim, C. Yoon, Y.-K. Park, and S. Kwon, "Automated adaptive frequency tracking system for efficient mid-range wireless power transfer via magnetic resonanc coupling," in *2012 42nd European Microwave Conference*, 221–224, Amsterdam, Netherlands, 2012.

[12] Tan, P.-A., H. He, and X. Gao, "A frequency-tracking method based on a SOGI-PLL for wireless power transfer systems to assure operation in the resonant state," *Journal of Power Electronics*, Vol. 16, No. 3, 1056–1066, 2016.

[13] Li, Y., C. Zhang, Q. Yang, J. Li, Y. Zhang, X. Zhang, and M. Xue, "Improved ant colony algorithm for adaptive frequency-tracking control in WPT system," *IET Microwaves, Antennas & Propagation*, Vol. 12, No. 1, 23–28, 2018.

[14] Li, Y., L. Liu, C. Zhang, Q. Yang, J. Li, X. Zhang, and M. Xue, "Improved particle swarm optimization algorithm for adaptive frequency-tracking control in wireless power transfer systems," *Journal of Power Electronics*, Vol. 18, No. 5, 1470–1478, 2018.

[15] Lu, F., H. Zhang, H. Hofmann, and C. Mi, "A dual-coupled LCC-compensated IPT system to improve misalignment performance," in *2017 IEEE PELS Workshop on Emerging Technologies: Wireless Power Transfer (WoW)*, 1–8, Chongqing, China, 2017.

[16] Xiao, C., D. Cheng, and K. Wei, "An LCC-C compensated wireless charging system for implantable cardiac pacemakers: Theory, experiment, and safety evaluation," *IEEE Transactions on Power Electronics*, Vol. 33, No. 6, 4894–4905, 2018.

[17] Zhang, Y., Z. Yan, T. Kan, X. Zeng, S. Chen, and C. C. Mi, "Modeling and analysis of a strongly coupled series-parallel-compensated wireless power transfer system," *IEEE Journal*

of Emerging and Selected Topics in Power Electronics, Vol. 7, No. 2, 1364–1370, 2019.

[18] Zhang, Y., Z. Yan, Z. Liang, S. Li, and C. C. Mi, "A high-power wireless charging system using LCL-N topology to achieve a compact and low-cost receiver," *IEEE Transactions on Power Electronics*, Vol. 35, No. 1, 131–137, 2020.

[19] Khan, S. R., S. K. Pavuluri, and M. P. Y. Desmulliez, "Accurate modeling of coil inductance for near-field wireless power transfer," *IEEE Transactions on Microwave Theory and Techniques*, Vol. 66, No. 9, 4158–4169, 2018.

[20] Luo, Y., "Field and inductance calculations for coaxial circular coils with magnetic cores of finite length and constant permeability," *IET Electric Power Applications*, Vol. 11, No. 7, 1254–1264, 2017.

[21] Ke, Q., W. Luo, G. Yan, and K. Yang, "Analytical model and optimized design of power transmitting coil for inductively coupled endoscope robot," *IEEE Transactions on Biomedical Engineering*, Vol. 63, No. 4, 694–706, 2016.